Proceedings of the Canadian Society for Mechanical Engineering International Congress
32nd Annual Conference of the Computational Fluid Dynamics Society of Canada
Canadian Society of Rheology Symposium
CSME/CFDSC/CSR 2025
May 25–28, 2025, Montréal, Québec, Canada

A Computational Study Investigating the Influence a Co-Rotating Hub Retrofit has on Tidal Turbine Performance

Finley M. Corbett*, Tiger L. Jeans, Andrew G. Gerber,
Department of Mechanical Engineering, University of New Brunswick, Fredericton NB, Canada
*fcorbett@unb.ca

***Abstract*—**This paper numerically investigates how a retrofitted hub geometry affects the power extraction of a Horizontal Axis Tidal Turbine (HATT) using Computational Fluid Dynamics (CFD). At the root region of traditional HATTs, the blade transitions from a hydrofoil to a circular cross-section for structural and operational requirements. This leads to a local low lift to drag ratio experienced by the blades. Minimizing this loss is the primary motivation of adding a hub retrofit. While an increase net power extraction was not observed using this preliminary design, the tangential force contribution of the main turbine blade was improved after adding the retrofit by 2.94%. Retrofit-induced hydrodynamic effects responsible for this tangential force increase include: the effect of the hub retrofit tip vortex, the increase in local angle of attack experienced by the primary blade root region, and the increase in horseshoe vortex circulation strength at the root to hub junction. The present work is a precursor to an optimization effort and will be used to establish baseline results and a workflow for future improvements.

***Keywords*—Computational Fluid Dynamics; Horizontal Axis Tidal Turbine; root loss; Blade Element Momentum**

I. INTRODUCTION

In recent years, significant attention has been given to coastal sites that experience ebb and flow tide conditions suitable for harnessing power. This is due to the evolution in technology that allows for the installation of turbomachinery in harsh tidal environments. An example of these tidal sites is Minas Passage in the Bay of Fundy, which has been examined both experimentally and numerically using regional bathymetry data to quantify its cyclical unsteady turbulent flows [1] and energy potential [2].

The most popular method for harnessing power in tidal cycles is done by using Horizontal Axis Tidal Turbines (HATTs). Although more commonly used to extract power from the wind (Horizontal Axis Wind Turbines or HAWTs), HATTs have the advantage of operating in predictable environments with significantly higher power densities. For both HATTs and HAWTs, electricity is produced through taking advantage of basic conservation of energy principles, converting the translational kinetic energy of the freestream environment into torque to turn a generator. To generate torque, the blades are oriented and designed to optimize the lift and drag ratio along the span. Given the strong dependence the hydrodynamics have on electrical output, considerable effort is placed in making the blades as efficient as possible.

A consistent major aerodynamic loss experienced by HATTs and HAWTs exists at the blade root. Due to structural and operational restrictions, the desired blade profile cannot continue into the lower radial locations of the span. Instead, the blade is blended into a cylindrical root which intersects with the hub, causing local low lift to drag ratios. This causes a loss in power extraction, which accounts for an approximate reduction of 5% in HAWT aerodynamic efficiency [3]. Since the blades are generating lift, helical root vortices are also present [4], contributing an induced root loss. Furthermore, root losses are exacerbated in HATTs as the cylindrical region occupies a proportionally larger spanwise region in comparison to HAWTs.

In an attempt to limit root losses, Rosendberg *et al.* [3] numerically investigated the performance of a Dual Rotor Wind Turbine (DWRT). Analogous to multi-stage turbomachinery, DWRTs contain two blade rows, with the upstream rotor having a smaller swept area. This allows for the recovery of the energy typically lost at the root of the primary (downstream) rotor. By exploring a parametric space of variable axial spacing, relative radii, and relative angular velocities, they found a maximum increase of 7% in power generation using an Actuator Disk (AD) methodology to model the turbine blades within a Computational Fluid Dynamics (CFD) domain. Zhu *et al.* [5] also attempted to reduce root losses in HAWTs using

Natural Sciences and Engineering Research Council of Canada (NSERC)
Biome Renewables®

additional geometry by placing a disk upstream of the main rotor. This disk introduces a convective radial acceleration in the flow, directing it onto the spanwise regions of the blade capable of locally generating significant torque. They found a maximum increase in power generation of 1.5% in a parametric space containing variations in axial separation and disk radius. Similarly to Rosendberg *et al.* [3], Zhu *et al.* [5] modelled the turbine blades using an AD methodology with a CFD domain. The Immersed boundary (IB) method was used to calculate source terms representative of a disk being placed upstream of the main rotor.

The present study assess the performance influence on an existing HATT using a novel co-rotating hub retrofit geometry. To accurately resolve the entire flowfield, Reynolds Averaged Navier Stokes (RANS) CFD simulations were conducted. This paper outlines the methodology used to obtain high-fidelity CFD solutions for the unaltered (standalone) HATT, the introduction of the hub retrofit into the CFD domain, and the primary retrofit-induced hydrodynamic effects responsible for changes in turbine performance.

II. GEOMETRY

The HATT investigated is the 18 m diameter ANDRITZ Hydro Hammerfest Mk1 turbine. To ground all forces, moments, geometry, and kinematics, the global coordinate system (X, Y, Z) is established in Fig. 1. The radial position, r, (co-planar with the Y and Z axes) is included as it will be used to define spanwise load distributions. The origin is defined as the intersection of the three blade pitching axes. The Z-axis is defined as the pitching axis of the vertically oriented blade. The positive X-axis is taken as the freestream direction, making the rotor plane of the turbine equivalent to the Y-Z plane at $X = 0$. Integrated hydrodynamic forces and moments are F_X, F_Y, F_Z and Q_X, Q_Y, Q_Z, respectively. Freestream velocity and the angular velocity of the rotating reference frame are given as U_∞ and Ω, respectively.

To characterize the geometry of the turbine blade, Fig. 2 provides the chord, c, and twist, θ, distributions as a function of r, normalized by blade radius, R. Chord is the local distance between the leading and trailing edges of the blades for equal

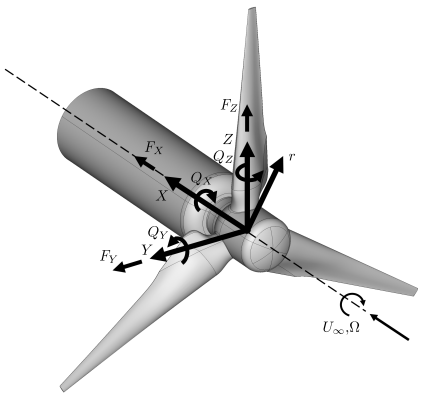

Figure. 1: HATT global coordinate system used to define forces, moments, and kinematics.

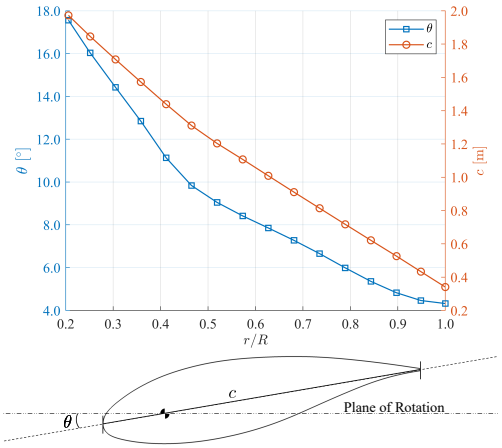

Figure. 2: HATT blade twist, θ, and chord, c, distributions taken at 11 spanwise locations. The blade cross section shown is at $r/R = 0.8$.

Z-locations. Twist is the angle between the chord line and the rotor plane.

Fig. 3a outlines the HATT hub retrofit geometry, which is divided into three regions: the nose, the tip, and the mid-span. Fig. 3b defines the mid-span geometry similarly to Fig. 2: retrofit chord, c_{RF}, and twist, θ_{RF}, distributions as a function of r, normalized by retrofit radius, R_{RF}. To define tangential and axial deflection of the retrofit, a double angle distribution is used as shown in Fig. 3c. These angles are defined as sweep (tangential deflection), Λ, and prebend (axial deflection), ζ.

III. COMPUTATIONAL METHODOLOGY

A. RANS Solver and Boundary Conditions

The steady-state CFD simulations performed to analyse the standalone turbine geometry and assess the influence of the hub retrofit were conducted using the commercial software, ANSYS CFX [6]. For the present study, this code was used

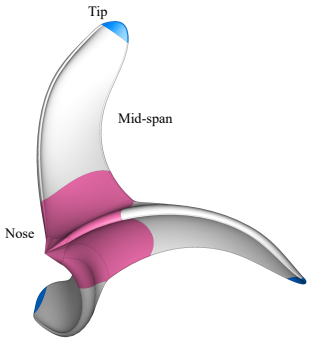

(a) Hub retrofit geometry. Nose, mid-span, and tip regions are identified.

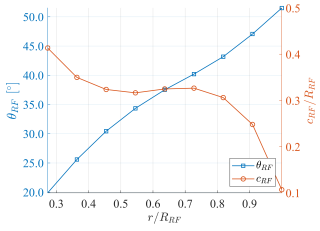

(b) θ_{RF} and c_{RF} distributions.

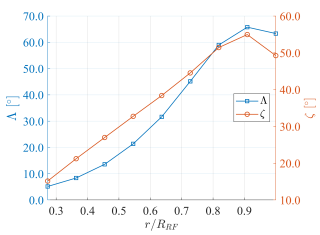

(c) ζ and Λ distributions.

Figure. 3: Retrofit geometry and distributions for twist, θ_{RF}, chord, c_{RF}, prebend, ζ, and sweep, Λ.

to apply the Finite Volume Method (FVM) to the incompressible RANS equations and k-ω Shear Stress Transport (SST) turbulence model [7] across stationary and rotating domains.

The boundary conditions applied are shown in Fig. 4 and were chosen to reflect an idealized tidal environment. They include a uniform velocity profile at the inlet, no-slip walls at the turbine geometry, an opening at the outlet, and a free-slip wall applied to the farfield. An inlet turbulence intensity of 5% was chosen, which broadly aligns with the experimental findings of Wilcox et al. [1], who reported ebb and flood streamwise turbulence intensities ranging between approximately 2.5-6% and 8-12%, respectively, in Grand Passage of the Bay of Fundy. Periodic interfaces are also introduced, allowing for 120° of the total geometry to be analysed. Lastly, a rotating reference frame is applied to simulate the rotating blades. This is enforced by splitting the CFD domain into two reference frames using General Grid Interfaces (GGIs) and the Frozen Rotor model.

B. Mesh Generation

To balance the desire for increased numerical accuracy and reduced mesh complexity, hybrid CFD meshes were produced using Fidelity Pointwise [8]. The grid topology created is comprised of a hexahedral interior (Fig. 5b and 5d), a tetrahedral transition (Fig. 5b and 5c), and a hexahedral farfield (Fig. 5a). The hexahedral interior consists of inflation layers and a block-structured wake. Inflations layers increase in cell height at a growth rate of 1.2 from the wall, extending far enough to completely resolve all boundary layers. Initial cell height was selected to approximate $y^+ = 1$ across the blade span, which is recommended when using ω-based turbulence models [6]. The tetrahedral transition is a coarser mesh region containing tetrahedral and pyramid elements, which allows for an efficient grid evolution to the hexahedral farfield.

Grid convergence was achieved by varying domain size to eliminate blockage effects, and by varying wake refinement to ensure induction phenomena are appropriately captured. The sensitivity study consisted of five different grids ranging from 30 to 45 million control volumes for the periodic domain. Turbine loads became independent of cell count at a mesh containing 36 million control volumes. This was the grid chosen for the computational study.

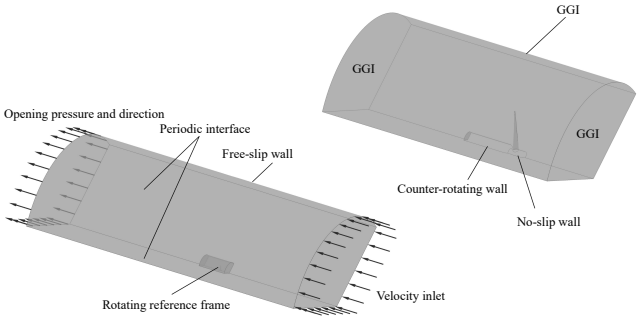

Figure. 4: Boundary conditions and interfaces in the simulations conducted. The upper right figure shows the rotating reference frame domain.

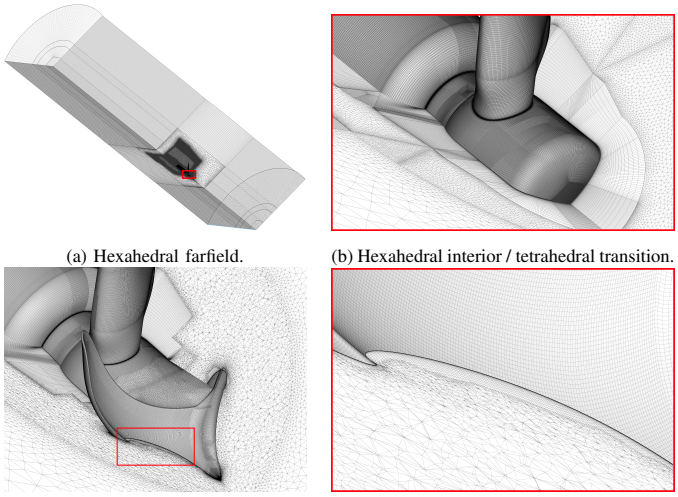

(a) Hexahedral farfield.

(b) Hexahedral interior / tetrahedral transition.

(c) Retrofit tetrahedral transition.

(d) Retrofit T-rex inflation layers.

Figure. 5: Standalone and retrofit-turbine coupling CFD mesh topologies. The grids are divided into three regions: the hexahedral interior, tetrahedral transition, and hexahedral farfield.

Considering the geometry of Fig. 3a exhibits features that are challenging to mesh manually, the automated T-rex algorithm was used to resolve retrofit boundary layers (Fig. 5c and 5d). By specifying parameters for growth rate, initial cell height, and the number of cell layers, T-Rex builds right-angle anisotropic tetrahedral elements from the wall, and combines them into hexahedra upon inflation layer completion [8].

IV. CFD PREDICTED HATT SIMULATIONS AND VERIFICATION

Simulations of the standalone HATT were conducted at nine different tip speed ratios (4.54, 4.69, 4.86, 5.13, 5.33, 5.74, 6.22, 6.79, and 7.47) to resolve the performance curve. Tip speed ratio, λ, is defined as follows,

$$\lambda = \frac{\Omega R}{U_\infty}. \tag{1}$$

For the case where $\lambda = 5.74$, a flowfield visualization is provided in Fig. 6 by identifying dominant vortical structures using isosurfaces and a total pressure contour along the X-Y plane. By adding two additional graphical instances to the periodic domain, clear tip and root vortices are present, indicating reasonable wake resolution.

To provide confidence in the CFD-predicted turbine loads, a Blade Element Momentum (BEM) code was developed. Although lower order models like BEM capture less physics and are therefore not as accurate as CFD, comparing a numerical result with momentum-based fluid mechanics theory and 2D hydrofoil data provides confidence that the results are reasonable. Furthermore, BEM has known limitations at the extremes of the performance curve. By carefully comparing the two methodologies, these limitations can be identified and used to indicate where the CFD predictions account for effects neglected or indirectly modelled in BEM.

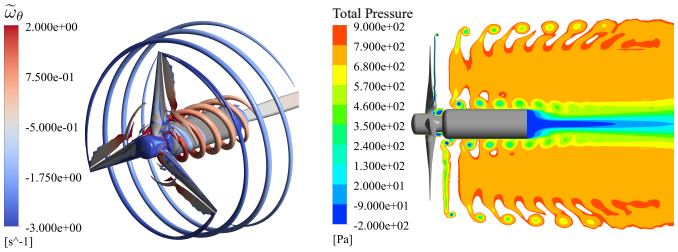

(a) Helical vortices. (b) Total pressure.

Figure. 6: The primary vortex structures and a streamwise total pressure contour along the X-Y plane for $\lambda = 5.74$. Helical vortices are shown using an isosurface at a Q-criterion of 1.2, coloured using the circumferential component of vorticity, $\widetilde{\omega}_\theta$. The total pressure contour is clipped such that only values under 810 Pa are visible.

Originally developed by Glauert [9], BEM functions by developing equations for spanwise blade torque and thrust distributions using a streamtube momentum balance and a 2D airfoil profile force analysis. Since the turbine is extracting power, the wake experiences a velocity deficit, which influences the relative flow angles experienced by the turbine blades. This influence is quantified in terms of axial and tangential induction factors, which are treated as unknowns in the equations for torque and thrust. Induction factor distributions can then be solved iteratively to yield turbine load predictions. Momentum-based torque and thrust equations are provided as (2) and (3), and 2D airfoil torque and thrust equations are provided as (4) and (5). Induction factor equations are obtained by equating (2) to (4) and (3) to (5), to obtain (6) and (7) [10].

$$dT = 4Fa(1-a)\rho {U_\infty}^2 \pi r dr \tag{2}$$

$$dQ = 4Fa'(1-a)\rho U_\infty \Omega \pi r^3 dr \tag{3}$$

$$dT = \frac{\sigma' \pi \rho U_\infty^2 (1-a)^2 \left[C_l \cos(\phi) + C_d \sin(\phi)\right] r dr}{\sin^2 \phi} \tag{4}$$

$$dQ = \frac{\sigma' \pi \rho U_\infty^2 (1-a)^2 \left[C_l \sin(\phi) - C_d \cos(\phi)\right] r^2 dr}{\sin^2 \phi} \tag{5}$$

$$a = \left[\frac{4F \sin^2 \phi}{\sigma'(C_l \cos\phi + C_d \sin\phi)} + 1\right]^{-1} \tag{6}$$

$$a' = \left[\frac{4F \sin\phi \cos\phi}{\sigma'(C_l \sin\phi - C_d \cos\phi)} - 1\right]^{-1} \tag{7}$$

Variables introduced in (2) - (7) include the thrust and torque on an annular segment of the rotor plane, dT and dQ, the width of the annular segment, dr, axial and tangential induction factors, a and a', blade solidity, σ', lift and drag coefficients of a 2D airfoil for the given radial position, C_l and C_d, relative flow angle, ϕ, and Prandtl's correction factor for helical tip and root vortices, F. The full development of this theory is available in Manwell *et al.* [10]. Limitations present in BEM include uncertainties in the 2D sectional data for boundary layer separation and root region predictions, Prandtl's reduced order model used to calculate helical vortex contributions, the invalidity of the momentum theory for $a > 0.5$ (Turbulent Windmill State or TWS) [11], and spanwise flow effects [12], [13].

To compare the CFD and BEM predictions for the HATT of the present study, non-dimensionalized values for power and thrust are provided in Fig. 7. These coefficients are obtained from dimensional analysis and are given as follows,

$$C_{\widetilde{P}} = -\frac{\widetilde{P}}{\frac{1}{2}\rho A {U_\infty}^3} = -\frac{\Omega Q_X}{\frac{1}{2}\rho A {U_\infty}^3}, \tag{8}$$

and

$$C_T = \frac{T}{\frac{1}{2}\rho A {U_\infty}^2} = \frac{F_X}{\frac{1}{2}\rho A {U_\infty}^2}, \tag{9}$$

where $\widetilde{P}$ is the total extracted mechanical power, T is the total thrust, A is the swept rotor area, and ρ is the fluid density. The two methods show good agreement, particularly for mid-range λ values. For higher values of λ, BEM over predicts $C_{\widetilde{P}}$, which can be attributed to the TWS, as spanwise a-distributions are proportional to λ [10]. Even though empirical corrections are present in BEM to account for high-induction states, most models used show a generally poor correlation to experimental results [11]. At lower values of λ, a deficit in the BEM predictions for thrust is present, which can be attributed to the uncertainty in 2D hydrofoil data. In the present study, the viscous mode of XFOIL was used to collect the lift and drag curves for 20 cross sections of the HATT. Considering more boundary layer separation will be present at low values of λ, and XFOIL is not suitable for accurate boundary layer separation predictions, it is the uncertainty in 2D data causing the BEM thrust deficit.

Spanwise force distributions can also be compared between BEM and CFD methodologies, as shown in Fig. 8 for $\lambda = 5.74$. Distributions per unit span are provided for thrust, f_X, tangential force, f_Y, bending moment, q_Y, and torque, q_X.

V. RESULTS AND DISCUSSION

With the standalone turbine CFD simulations obtained and compared to theoretical results, the influence of the hub-retrofit

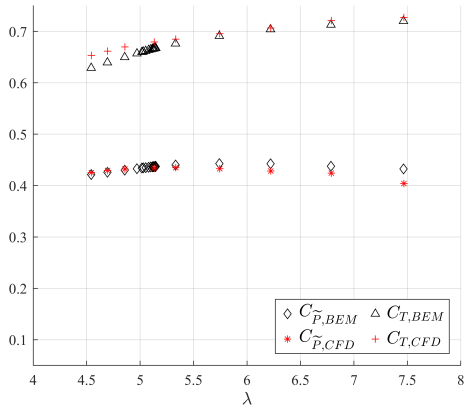

Figure. 7: CFD and BEM predictions of power and thrust for the HATT operating range.

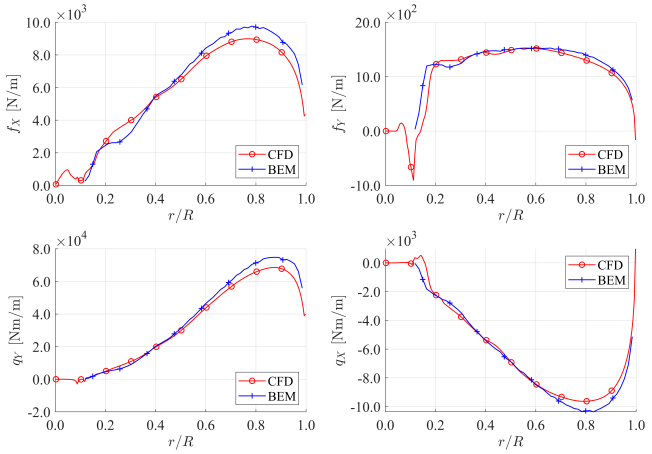

Figure. 8: CFD and BEM comparison of spanwise load distributions for thrust, f_X, tangential force, f_Y, bending moment, q_Y, and torque, q_X, at $\lambda = 5.74$.

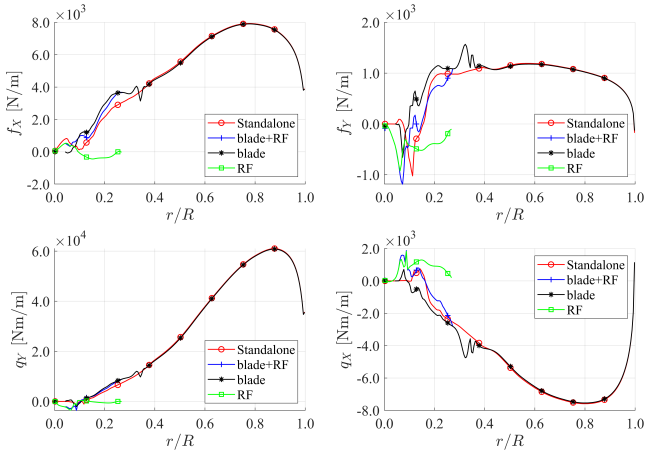

Figure. 9: Spanwise load for thrust, f_X, tangential force, f_Y, bending moment, q_Y, and torque, q_X, at $\lambda = 6.22$. Distributions are provided for the standalone turbine (Standalone), the retrofit-turbine coupling (blade+RF), the isolated blade with the influence of the retrofit (blade), and the retrofit (RF).

can be assessed. The selection of λ, retrofit positioning, and retrofit scale presented in this paper is based on a parametric study that evaluated combinations of λ, axial spacing, relative angle, and relative radius of the retrofit-turbine coupling. Table I presents $C_{\widetilde{P}}$ and C_T results for the best case simulated in the parametric study, compared to the standalone turbine at the corresponding λ ($\lambda = 6.22$).

To describe $C_{\widetilde{P}}$ and C_T for the standalone geomerty, the geometry after adding the retrofit, and the contributions of the isolated turbine blade, the respective subscripts i, f, and $blade$ are introduced. For example, the power coefficient before adding the retrofit, the power coefficient after adding the retrofit, and the power coefficient of the isolated blade after adding the retrofit are expressed as $C_{\widetilde{P},i}$, $C_{\widetilde{P},f}$, and $(C_{\widetilde{P},f})_{blade}$, respectively.

No net improvement in power extraction was achieved, as $C_{\widetilde{P},f} < C_{\widetilde{P},i}$. However, when investigating only the influence on the blade, power extraction was improved by 2.94%. Considering this increase, it can be concluded that the net decrease in performance is due to the adverse torque contributions of the retrofit. To determine where local improvement occurs on the primary blade, spanwise load distributions before and after adding the retrofit are provided in Fig. 9. Similarly to the load coefficients described in Table I, the spanwise loadings are given for the standalone rotor (Standalone), the rotor after the retrofit is added (blade+RF), and the isolated performance of the blade accounting for the hydrodynamic influence of the retrofit, ignoring the direct load contributions of the retrofit (blade). Also included are the load distributions of the retrofit itself (RF). Note that the blade+RF and blade predictions merge just above the retrofit tip. This occurs at $r/R = 0.27$.

TABLE. I
$C_{\widetilde{P}}$ AND C_T RESULTS FOR THE STANDALONE TURBINE GEOMETRY AND THE HUB RETROFIT-TURBINE COUPLING AT $\lambda = 6.22$.

$\boldsymbol{\lambda = 6.22}$					
$\boldsymbol{C_{\widetilde{P},i}}$	$\boldsymbol{C_{\widetilde{P},f}}$	$\boldsymbol{(C_{\widetilde{P},f})_{blade}}$	$\boldsymbol{C_{T,i}}$	$\boldsymbol{C_{T,f}}$	$\boldsymbol{(C_{T,f})_{blade}}$
0.4284	0.4204	0.4410	0.7065	0.7137	0.7164

Confirming the conclusion that the retrofit is generating adverse torque, the RF prediction shows a negative f_Y distribution. The most significant improvement on the primary blade occurs at $r/R = 0.32$, shown by the peak in f_Y (or trough in q_X). This can be attributed to the retrofit tip vortex interacting with the suction side and leading edge of the primary blade, increasing the local kinetic energy of the flow. As a result, the static pressure is reduced, increasing the local tangential force generated, contributing to the increase of $(C_{\widetilde{P},f})_{blade}$ from $C_{\widetilde{P},i}$. Fig. 10 depicts the evolution of this vortex using planes coloured with the Y-component of vorticity, $\widetilde{\omega}_Y$, normalized by the rotor plane radius and freestream velocity.

Although this tip vortex effect contributes to the influence at $r/R = 0.32$ in Fig. 9, f_Y is also increased from $r/R = 0.1$ to $r/R = 0.25$. This is due to the retrofit accelerating the incoming flow at the turbine blade root, and due to the retrofit causing an increase in strength of the primary blade horseshoe vortex at the hub to root junction.

Significant flow acceleration is present because the retrofit experiences a negative angle of attack, α_{RF}. Fig. 11 outlines this by showing a pressure contour and surface streamlines

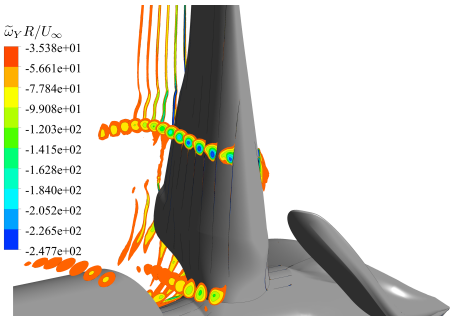

Figure. 10: Retrofit tip vortex contours along X-Z planes at 13 equally spaced Y-locations. Planes are coloured with the Y-component of vorticity, $\widetilde{\omega}_Y$, and are clipped such that only regions below $\widetilde{\omega}_Y R/U_\infty = -35.4$ are visible.

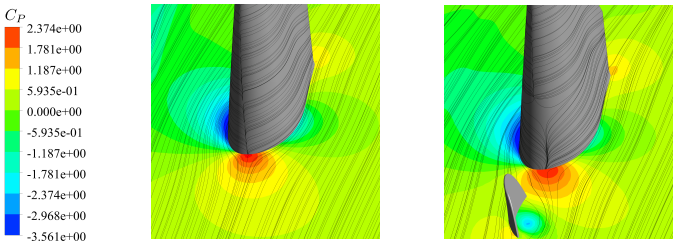

(a) Standalone. (b) With retrofit.

Figure. 11: A pressure coefficient contour ($C_P = 2P/\rho U_\infty^2$, where P is the static pressure) and surface streamlines at $r/R = 0.217$ to describe the change in relative flow angle after adding the retrofit. Surface streamlines on the blade are shown to indicate a shift in stagnation point.

along an X-Y plane. This results in a decrease in static pressure at the retrofit lower surface, increasing the kinetic energy just upstream of the primary blade leading edge. Additionally, the stagnation point from approximately $r/R = 0.15$ to $r/R = 0.25$ is shifted, indicating an increase in relative flow angle. Consequently, f_Y along the blade increases, contributing to $(C_{\widetilde{P},f})_{blade}$ being greater than $C_{\widetilde{P},i}$. The negative α_{RF} causing this effect is generating negative lift, and is responsible for the negative RF prediction of f_Y in Fig. 9.

The increase in the existing primary blade horseshoe vortex circulation can be rationalized by considering the influence of the retrofit root vortex. Similarly to the primary blade, a root vortex will be generated by the retrofit in addition to the tip vortex. Fig. 12 shows this effectively increase the horseshoe vortex circulation strength, causing a local reduction in static pressure. This leads to the peak in f_Y at $r/R = 0.12$ shown in Fig 9.

VI. CONCLUSIONS

This study investigated the effect a co-rotating hub retrofit has on the performance of an HATT, using a RANS CFD simulation methodology. To establish a performance baseline of the standalone turbine, CFD simulations were conducted over an operating range from $\lambda = 4.54$ to $\lambda = 7.47$ and compared with BEM. Good agreement was obtained between the CFD and BEM predictions, particularly for mid-range values of λ. Expected discrepancies between the two methodologies were present, primarily due to high induction states (TWS), and uncertainties in XFOIL predictions for the root region hydrofoils and boundary layer separation.

While a net power extraction increase was not observed after implementing the unoptimized retrofit design, valuable insight into the retrofit-induced flow effects responsible for increasing tangential blade load was obtained. This includes the effects of the retrofit tip vortex, the retrofit negative angle of attack, and the strengthening of the primary blade horseshoe vortex. The tip and horseshoe vortex effects of Fig. 10 and Fig. 12 both reduced the static pressure at the leading edge and suction side of the primary blade, yielding local peaks in f_Y. The negative α_{RF} effect accelerated the flow and increased the effective angle of attack of the primary blade, leading to an evenly distributed increase in f_Y from $r/R = 0.15$ to $r/R = 0.25$.

This study is a precursor to an on-going optimization effort which will attempt to improve the hydrodynamic performance of the retrofit. It serves as a workflow and a reference for anticipated flow physics that will exist in the optimized design.

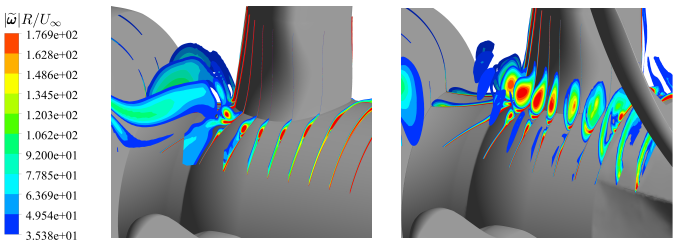

(a) Standalone. (b) With retrofit.

Figure. 12: Horseshoe vortex contours before and after adding the retrofit. Contours are shown on 11 planes, 7 of which are normal to the local axis of rotation of the horseshoe vortex. The four remaining planes are Y-Z planes to show the evolution of the vorticity generated by the region of high curvature caused by the retrofit-hub connection. All planes are coloured with vorticity magnitude, $|\widetilde{\omega}|$, and are clipped such that only regions above $|\widetilde{\omega}|R/U_\infty = 35.4$ are visible.

ACKNOWLEDGMENT

The authors acknowledge the Natural Sciences and Engineering Research Council of Canada (NSERC) and Biome Renewables® for their valuable contributions toward this work.

REFERENCES

[1] K.W. Wilcox, J.T. Zhang, I.M. McLeod, A.G. Gerber, T.L. Jeans, J. McMillan, A. Hay, R. Karsten, and J. Culina, "Simulation of device-scale unsteady turbulent flow in the Fundy Tidal Region," Ocean Engineering, vol. 145, pp. 59–76, 2017.

[2] R. H. Karsten, J. M. McMillan, M. J. Lickley, and R. D. Haynes, "Assessment of tidal current energy in the Minas Passage, Bay of Fundy," Proc. Inst. Mech. Eng. Part A J. Power Energy, vol. 222, pp. 493—507, 2017.

[3] A. Rosendberg, S. Selvaraj, and A. Sharma, "A novel dual-rotor turbine for increased wind energy capture," Journal of Physics, vol. 14, 2014.

[4] I. Herraez, B. Akay, and G. van Bussel, "Detailed analysis of the blade root flow of a horizontal axis wind turbine," Wind Energy Sci., vol. 1, 2016

[5] W. J. Zhu, W. Z. Shen, J. N. Sørensen, and H. Yang, "Verification of a novel innovative blade root design for wind turbines using a hybrid numerical method," Energy, vol. 141, pp 1661-1670, 2017.

[6] ANSYS, ANSYS CFX-Solver Theory Guide, Canonsburg, PA: ANSYS Inc, 2022.

[7] F. Menter, "Improved two-equation k turbulence models for aerodynamic flows," Technical Report, National Aeronautics and Space Administration, October, 1992.

[8] Cadence, Fidelity Pointwise User Manual, Cadence Design Systems Inc., 2024.

[9] A. Glauert, " The elements of aerofoil and airscrew theory," Cambridge University Press, 1926.

[10] J. F. Manwell and J. G. McGowan, "Wind Energy Explained," West Sussex, United Kingdom: John Wiley and Sons Ltd., 2009.

[11] M. L. Buhl, "A new empirical relationship between thrust coefficient and induction factor for the turbulent windmill state," Technical Report NREL/TP-500-36834, National Renewable Energy Laboratory, August, 2009.

[12] H. Snel, R. Houwink, and J. Bosschers, "Sectional prediction of lift coefficients on rotating wind turbine blades in stall," Technical report, Netherlands Energy Research Foundation, 1993.

[13] C. Lindenburg, "Modelling of rotational augmentation based on engineering considerations and measurements," European Wind Energy Conference, 2004.